ELSEVIER

Contents lists available at ScienceDirect

Acta Materialia

journal homepage: www.elsevier.com/locate/actamat



Full length article

Microstructure development and morphological transition during deposition of immiscible alloy films



Yong Lu^{a,b,*}, Benjamin Derby^c, Hariharan Sriram^b, Kamal Kadirvel^b, Cuiping Wang^a, Xingjun Liu^a, Amit Misra^{c,*}, Yunzhi Wang^{b,*}

- ^a College of Materials and Fujian Provincial Key Laboratory of Materials Genome, Xiamen University, Xiamen 361005, PR China
- b Department of Materials Science and Engineering, The Ohio State University, 2041 College Road, 477 Watts Hall, Columbus, OH 43210, USA
- ^c Department of Materials Science and Engineering, University of Michigan, Ann Arbor, MI, USA

ARTICLE INFO

Article history:
Received 1 November 2020
Revised 13 August 2021
Accepted 9 September 2021
Available online 15 September 2021

Keywords: Immiscible alloy Microstructural patterns Thin films Phase-field method

ABSTRACT

Complex three-dimensional microstructural patterns arise during deposition of immiscible alloys and their morphologies depend sensitively on alloy composition, deposition rates and substrate temperatures. Using phase field simulations, we construct a microstructure morphology map in a multidimensional space of material properties and processing parameters. We consider simultaneous effects from temperature-dependent surface and bulk diffusivities and thermodynamic driving force for phase separation, temperature- and composition-dependent interphase boundary and surface energies, as well as alloy composition, substrate temperature and deposition rate. The microstructural patterns and morphological transition sequences in as-deposited films revealed by the microstructure map are validated using experimental data from sputtered Cu-Mo alloy films as well as from other systems. Such a microstructural map can guide synthesis of three-dimensional compositionally modulated nanostructures via self-organization during deposition of immiscible alloy films.

© 2021 Acta Materialia Inc. Published by Elsevier Ltd. All rights reserved.

1. Introduction

Thin films with periodic concentration modulations (CM) have attracted considerable attention lately because of technological applications found in, for example, field-effect transistors [1], photodetectors [2], energy storage [3], and phase change random access memory [4]. Films with vertical CM (VCM, where vertical refers to the direction that is perpendicular to the film, *i.e.*, parallel to the growth direction) and lateral CM (LCM) have been shown to exhibit unique electronic band structures, electrical carrier mobility and phase transformation characteristics. They offer tremendous benefits for the design of functional devices with large excitonic effect, bandgap modulation, indirect to direct bandgap transition, piezoelectricity and valleytronics [5–7]. They also exhibit novel structural properties and radiation damage tolerance behavior [8,9].

Fabrication of CM films by alternating deposition can hardly control the modulation wavelength and film morphology in three dimensions (3D). On the other hand, phase separation during codeposition of immiscible alloy films with a large positive enthalpy

E-mail addresses: luyong@xmu.edu.cn (Y. Lu), amitmis@umich.edu (A. Misra), wang.363@osu.edu (Y. Wang).

of mixing enables low-cost batch fabrication of self-organized 3D nanoscale morphological patterns [10,11] and has been utilized widely in producing films with various uniform spatial CM patterns having desired physical properties [12-15]. Depending on the concave downward part of the free energy surface in either the compositional space, structural space, or both, the phase separation may occur by either the spinodal decomposition (isostructural) or de-mixing (heterostructural) mechanism. Previous studies have demonstrated that the development of directional CM patterns is determined by the interplay between phase separation kinetics and film deposition rate and substrate temperature [16-20], which have been utilized successfully in the design of self-organized CM films in various devices [21,22]. According to the theoretically predicted "isothermal microstructure map" [18], the spinodal decomposition process during co-deposition could be controlled in the processing parameter space to produce various microstructural patterns via morphological transition from one type to another.

A number of recent investigations have highlighted morphological control in co-deposited thin films at different deposition temperatures. Nano-lamellar TiN/AlN films and multilayer TiO_2/VO_2 films have been prepared via spinodal decomposition at 800 °C, at which bulk diffusion is relatively slow in these ceramic systems [15]. Derby et al. [16,23] showed that Cu-Mo films with all three

^{*} Corresponding authors.

types of CM microstructures, i.e., VCM, LCM and random concentration modulation (RCM) structures can be fabricated under the same deposition rate, e.g., 1.4 nm/s, but at different temperatures. Xie et al. reported [24] a series of self-organized binary immiscible Cu-X (X:W, Mo, Nb, V, Cr, Al) films with VCM structures prepared at low temperatures. These experimental studies represent an uncharted territory for theoretical modeling and computer simulations because the "isothermal microstructure map" developed in the literature [18], without considering the temperature effect, cannot be applied to these cases. For example, according to the isothermal microstructure map [18], the VCM formation requires a relatively fast rate of phase separation (compared to the deposition rate) via bulk diffusion [18,25], which is most unlikely to be the case at low temperatures because the sluggish bulk diffusion and faster surface diffusion may not be able to give rise to the precursory "chessboard structure" that leads to VCM after coarsening. Cu-X (where X is a BCC refractory metal) binary alloys have rather small interdiffusivities $(10^{-16} \sim 10^{-13} \text{ cm}^2/\text{s} \text{ from } 500)$ to 700 °C) in bulk at low deposition temperatures [26]. Thus, the formation mechanisms of VCM in Cu-X films at low temperatures cannot be explained by the mechanisms revealed by the isothermal microstructure map either. Furthermore, the fast bulk diffusion at high temperatures could enhance coarsening and interrupt the continuous growth of LCM along the film growth direction. A more recent study [27] did consider the surface diffusion effect, but came short of predicting the VCM structure at low tempera-

During co-deposition, mechanically mixed alloy layers are continuously added on the surface of a growing film, which subsequently undergo phase separation. Thus, the deposition rate determines the thickness of freshly added surface layers. The kinetics of phase separation relative to the deposition rate is extremely sensitive to the substrate temperature. Using a regular solution model as an example, which characterizes an alloy system with of a miscibility gap, the temperature-dependent free energy hump between the two equilibrium compositions reflects the driving force for spinodal decomposition. The lower of the temperature, the higher of the free energy hump and hence the larger of the driving force for phase separation. However, both bulk and surface diffusivities are significantly lower at low temperatures, thereby limiting the kinetics of phase separation during deposition. Furthermore, the bulk diffusivity becomes significantly lower than the surface diffusivity at low temperatures, which may alter the evolution pathway for CM development. In previous models, the temperature dependences of the thermodynamic driving force and ratio of surface vs. bulk diffusivities were not considered. Therefore, these models may not be able to capture surface-diffusion-, bulkdiffusion- or mixed surface-diffusion + bulk-diffusion-controlled phase separation processes, and thus the true balance between phase separation kinetics and deposition rate that determines the experimentally observed CM patterns. At the same deposition rate, bulk-diffusion will dominate the phase separation kinetics at high temperatures while surface diffusion will make significant contributions to the phase separation process. In addition, when the two phases have different surface energies, the phase with lower surface energy will prefer to form at the film surface [28]. This effect drives interdiffusion of atoms in the vertical direction (perpendicular to the film) in the surface and subsurface layers and gives rise to a VCM structure [29].

In this study, using a combination of phase field simulation and experimental characterization of sputtered immiscible alloy films, we investigate morphological pattern formation and transition during film deposition in a multi-dimensional space of materials and processing parameters, including temperature-dependent surface and bulk diffusivities, temperature-dependent thermodynamic driving force for phase separation, as well as temperatureand composition-dependent interfacial and surface energies. Based on the simulation results, the relationships among the types of CM patterns and the deposition rate, deposition temperature and alloy composition are established and documented in a microstructure map that is then validated against the experimental data. Similar to phase diagrams and TTT/CCT diagrams for alloy microstructure design, such a microstructure map is useful for the design of self-organization of CM patterns during deposition of immiscible alloys.

2. Methods

2.1. Phase-field model

For simplicity and without losing generality, we consider an A-B binary system with a miscibility gap. A structural order parameter η is introduced to distinguish solid from vapor, with $\eta = 0$ and $\eta = 1$ representing the vapor and solid phases, respectively, and $0 < \eta < 1$ representing the film surface. Assuming no lattice mismatch between the two co-existing phases (*i.e.*, no coherency elastic strain), the total free energy of the system can be formulated on the basis of the gradient thermodynamics [30]:

$$F = \int_{V} \left\{ f(c, \eta) + \frac{\kappa_c}{2} \nabla^2 c + \frac{\kappa_\eta}{2} \nabla^2 \eta \right\} dV$$
 (1)

where c is the solute concentration and κ_c and κ_η are the gradient energy coefficients for concentration and structure order parameters, respectively. $f(c,\eta)=h(\eta)~G^{chem}+(1-h(\eta))~G^{gas}$ is the local chemical free energy with $h(\eta)=\eta^4/4-\eta^3/3$, G^{chem} is approximated by a regular solution model and can be written as: $G^{chem}=RT(c\ln(c)+(1-c)\ln(1-c))+L_{mix}c(1-c)$, where R is the gas constant, T is temperature and L_{mix} is the enthalpy of mixing. G^{gas} is the free energy of the vapor phase, approximated by a parabola, i.e., $G^{gas}=(c-c_0^g)^2$.

The temporal evolutions of the structural order parameter field and concentration field during film deposition and phase separation processes are governed respectively by the Allen-Cahn and Cahn-Hilliard equations [31,32]:

$$\frac{\partial \eta}{\partial t} = -L \left(\frac{\partial f}{\partial \eta} - \kappa_{\eta} \nabla^{2} \eta \right) \tag{2}$$

$$\frac{\partial c}{\partial t} = \nabla \left[M(c, \eta) \nabla \left(\frac{\partial f}{\partial c} - \kappa_c \nabla^2 c \right) \right]$$
 (3)

Where $M(\eta)=\eta M_{\rm b}+(1-\eta)M_{\rm s}$ is the chemical mobility. The mobilities in the bulk and surface area, $M_{\rm b}(c)$ and $M_{\rm s}(c)$, can be obtained by the inter-diffusivities, *i.e.*,

$$M_b(c,T) = \frac{D_b(c,T)}{\partial^2 f/\partial c^2} \tag{4}$$

$$M_s(c,T) = \frac{D_s(c,T)}{\partial^2 f/\partial c^2}$$
 (5)

where $\widetilde{D_b}(c,T)=cD_b^A(T)+(1-c)D_b^B(T)$ and $\widetilde{D_s}(c,T)=cD_s^A(T)+(1-c)D_s^B(T)$ with D_b^i and D_s^i (i=A,B) representing intrinsic-diffusivities of component i in the bulk and at the surface, respectively. For simplicity, $D_b^A(T)=D_b^B(T)=D_b(T)$ and $D_s^A(T)=D_s^B(T)=D_s(T)$ were assumed. The temperature-dependences of the bulk and surface diffusivities are described by the Arrhenius-type relationships, i.e., $D_b(T)=D_b^0\exp(E^b/RT)$ and $D_s(T)=D_s^0\exp(E^s/RT)$, where D_s^0 and D_b^0 are the prefactors, E^b and E^s are the activation energies of bulk and surface diffusion, respectively. The kinetic coefficient, L, in Eq. (3) characterizes the deposition rate (i.e., growth rate of the film).

The film deposition process is simulated by continuously advancing a surface layer with an average composition of c_0 and a

Table 1The parameters used in the simulations.

Enthalpy of mixing, L_{mix}^*	22000/T+18.16
Gradient energy coefficient, $\kappa_c^* \kappa_\eta^*$	1.0
Dimensionless time step, Δt^*	1.0×10^{-3}
Grid size, $nx \times ny \times nz$	$256\times256\times128$
Prefactor of bulk diffusivity, D_s^0	1×10^{-10}
Prefactor of surface diffusivity, D_b^0	1×10^{-6}
Activation energies of bulk diffusion, E^b	-15000
Activation energies of surface diffusion, Es	-4000
Equilibrium composition of gas, c_0^g	0.5

structural order parameter of η = 1 in the growth direction. Under constant surface energy and given local chemical free energy $f(c, \eta)$, the surface layer thickness is controlled by the gradient energy coefficient, κ_{η} . A 3-dimensional (3D) system is considered, which contains 256*256*128 grid points. A periodical boundary condition is used in the horizontal direction and a zero-flux boundary condition is used at the vertical boundary. In all simulations the dimensionless grid spacing is chosen to be $\Delta x/l_0 = \Delta y/l_0 = \Delta z/l_0 = 1.0$, where l_0 is the grid size. The dimensionless deposition rate is given by $v^*=v/(l_0/\Delta t)$, where Δt is the time interval per simulation step. The chemical free energy is normalized by RT, i.e., $G_{Chem}^* = G_{Chem}/RT$, while $L_{mix}^* = L_{mix}/RT$. The intrinsic-diffusivities are normalized by the prefactor D_s^0 , i.e., $D_s^*(T) = \exp(E^s/RT)$ and $D_h^*(T) = (D_h^0/D_s^0) \exp(E^b/RT)$. The parameters used in the simulations are listed in Table 1. The plots of chemical free energy and the base ten logarithm of $D_s^*(T)/D_h^*(T)$ are shown in Fig. 1. It should be mentioned that the surface diffusion could be much faster than the bulk diffusion. During continuous deposition, surface diffusion only occurs within the film surface region that is quickly (depending on the deposition rate) buried by the newly deposited atoms and becomes bulk. Hence, the surface diffusivity in our simulation is different from the value measured from a free film surface without considering the deposition process. Based on the experimental measurements [26,33], $D_s^*(T)/D_h^*(T)$ is assumed to be no more than 3 orders of magnitude. The deposition temperature is normalized by the critical temperature of spinodal decomposition, e.g., $T^*=T/T_c$. The molar volumes of the two phases are assumed to be the same. Fig. 2 shows the calculated miscibility gap, spinodal and phase fraction contour lines by the thermodynamic parameters used in the simulation. The surface energy could be calculated by integrating the energy density in the surface area [34], which is the same for the A-rich and B-rich phases because of the free energy density curve is symmetrical with respect to c=0.5. The surface energy increases as solute concentration in the surface layer moves towards 0.5 (where the concentration gradient reaches maximum) and decreases with increasing temperature. During co-sputtering, if the two elements sputtered at equal deposition rates, the instantaneous composition of the film surface layer is close to 0.5. This thin surface layer (maybe a few atomic layers) can be treated as a "mechanically" mixed homogeneous solid solution. Due to the large positive entropy of mixing of immiscible alloys, there is a strong driving force for phase separation through bulk and surface diffusion. In addition, to account for surface defects and roughness [35], we have treated the surface layer as several grids (i.e., approximately 5 nm thick) where the surface diffusivity is applied. To quantitatively assess the spatial alignments of the various CMs obtained from the 3D phase field simulations, an inclination distribution of the interfaces was obtained by using Image[[36,37] analysis on multiple 2D vertical cross-sections. Based on the interface inclination distribution, the dominant interface inclination at the peak is chosen to distinguish the different types of CMs. The microstructures are now classified according to the following criteria: if the dominant interface inclination in a given microstructure has an angle around 0 degree with a horizontal line,

it is then classified as VCM, and if the dominant inclination has an angle of 90° with a horizontal line, it is then classified as LCM, otherwise the microstructures are classified as RCM.

2.2. Experiment

Immiscible alloys were co-deposited onto thermally oxidized Si substrates by DC magnetron sputtering in a Kurt J Lesker PVD 75 deposition system. The details of this deposition may be found in our previous work [16]. Chemical and microstructural characterization was used to link the morphologies and the processing parameters. Scanning/transmission electron microscopy (S/TEM) foils were prepared using focused ion beam (FIB) milling techniques in a TFS Helios 650 Nanolab SEM/FIB and a TFS Nova 200 Nanolab SEM/FIB. The foils were lifted out and attached to either Si or Mo grids to prevent interference during chemical composition scans. After thinning, the samples were plasma cleaned for a period of 5–8 min prior to S/TEM characterization. The samples were characterized using a JEOL 3100R05 double-Cs corrected S/TEM. The JEOL 3100 R05 was operated at 300 keV to achieve a point-to-point resolution of 0.055 nm for HAADF and BF imaging. The convergent angle for all image collection 111° with a camera length of 8 cm to true Z-contrast HAADF imaging. Energy dispersive X-ray spectroscopy (EDS) compositional maps were collected using a JEOL SDD X-ray detector with a 60 mm² active area.

3. Results

By introducing the temperature dependences of the thermodynamic parameters in the free energy model and the surface and bulk diffusivities, together with the dependence of surface energy on composition in the phase field model, we have simulated microstructure evolution during film deposition with different initial compositions at different deposition rates ($v^*=0.01\sim6$) and temperatures $(T^*=T /T_c)$. The equilibrium solute concentrations of the two phases at different temperatures are symmetrical with respect to 0.5, which implied that, by reversing the A-rich and B-rich phases, the microstructure evolutions for initial composition $0.5+\Delta c$ or $0.5-\Delta c$ are equivalent. Fig. 3 shows the as-deposited microstructures of the films. At a relatively high temperature, i.e. T*=0.8, a clear morphological transition from $LCM \rightarrow LCM + VCM \rightarrow VCM$ is observed with increasing deposition rate when the alloy composition c_0 is close to 0.5, coincide well with the results reported in the literature [18]. At this temperature, the difference between surface and bulk diffusion is relatively small and the surface energies of the two equilibria phases (that have compositions symmetrical to the average composition) are the same, which is close to the cases considered in the "isothermal microstructure map" [18]. However, there is a transition layer (with incomplete phase separation) near the bottom of the film in the VCM structure at higher deposition rates.

When the initial alloy composition moves away from $c_0 = 0.5$, e.g., $c_0 = 0.4$, 0.3 and 0.2, the VCM structure forms at smaller and smaller deposition rate and the individual layers become better aligned (e.g., almost perfect layered structures are found at high deposition rates in these alloys). The volume fraction (i.e., thickness) of the A-rich phase layers (blue) increases significantly at low deposition rate when the alloy composition moves away from $c_0 = 0.5$. However, at higher deposition rates, the volume fraction (i.e., thickness) of the A-rich and B-rich layers become similar, indicating that the composition in each layer deviates significantly from the equilibrium ones. These features have not been reported in previous studies [18,23,27].

At lower temperature and equal volume fraction (e.g., c_0 = 0.5), the CM morphology transforms from LCM \rightarrow VCM \rightarrow a non-decomposed ("frozen") state that gradually develop from the bot-

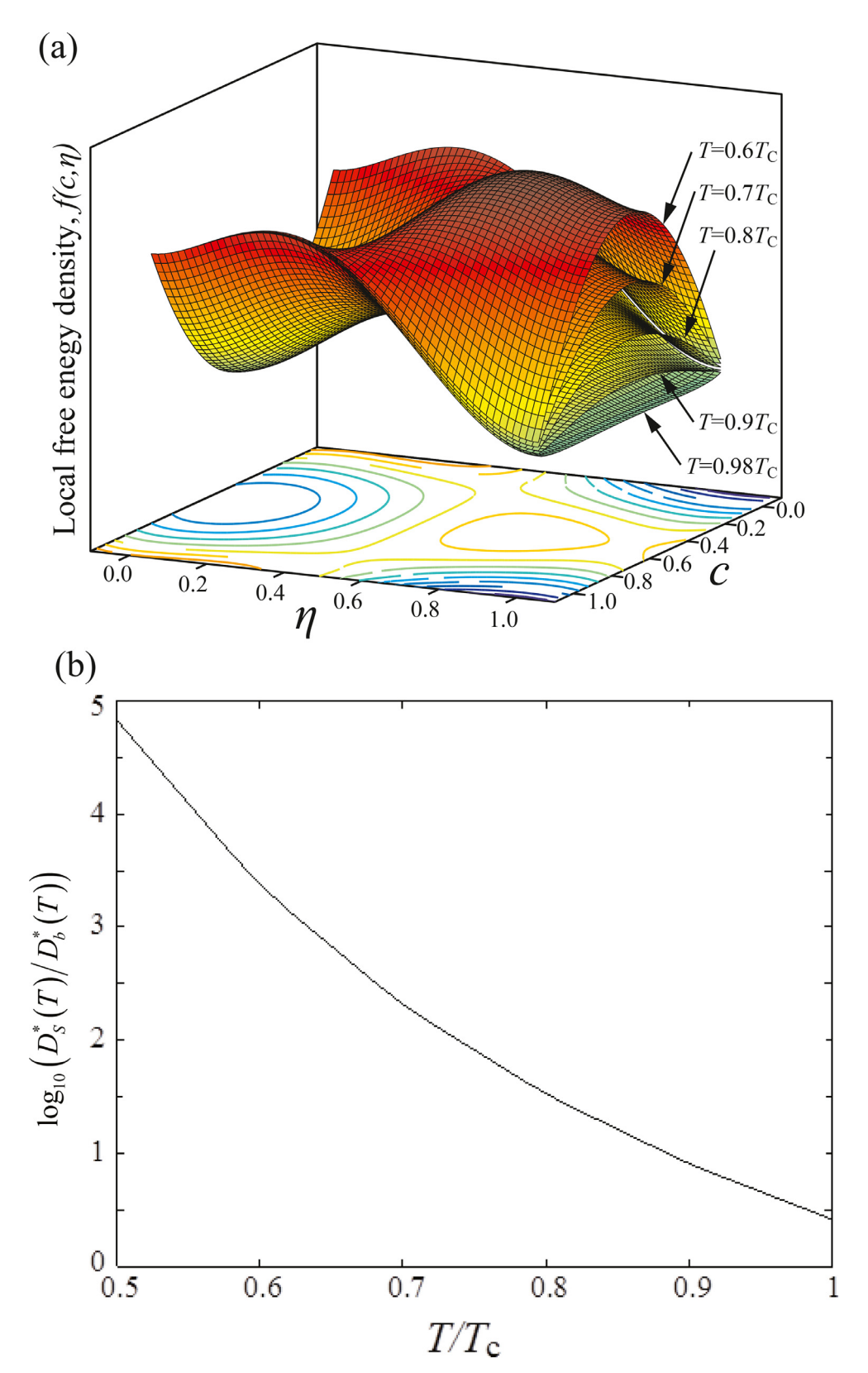


Fig. 1. The chemical free energy of the system (a) and the base ten logarithmic scale plot of as a function of T/Tc (b).

tom of the film as a function of increasing deposition rate. When the alloy composition moves away from $c_0 = 0.5$, volume fractions of the A-rich and B-rich layers become different. Again, the VCM structures are better developed when the alloy composition moves away from $c_0 = 0.5$ and perfect multi-layer structures can be found

in alloys having c_0 = 0.4, 0.3 and 0.2. At higher deposition rates, phase-separation does not occur at this relatively lower deposition temperature. As can be seen from Fig. 1(b), surface diffusion is much faster than bulk diffusion at T^* = 0.6 and, thus, it makes significant contributions to the phase separation process. The effec-

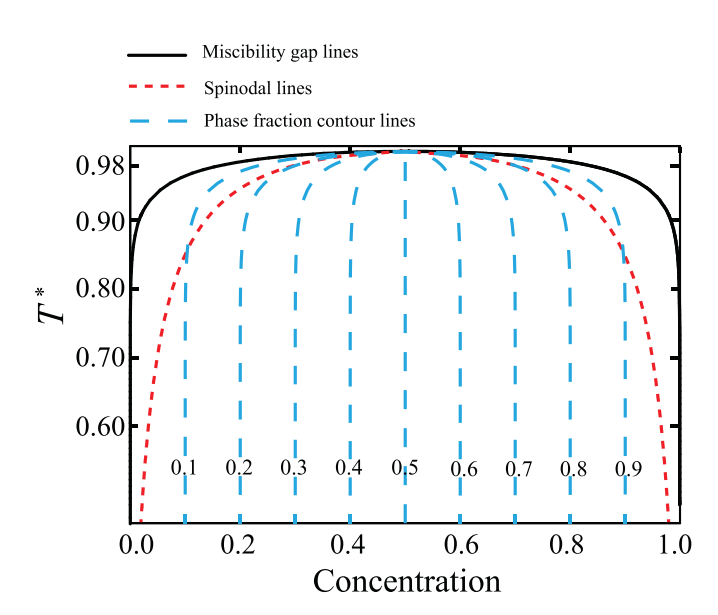


Fig. 2. Calculated miscibility gap, spinodal and phase fraction contour lines by the thermodynamic parameters used in the simulation.

tive depth of surface diffusion (\sim 5 nm) used in the present work is based on the experimental and theoretical analysis [38,39]. Contiguous growth of the two-phase regions beneath the surface area is insignificant due to the sluggish bulk diffusion. Compared with the microstructures developed at $T^*=0.8$, the compositions of the A-rich and B-rich phases are far away from equilibrium. Despite of the temperature change, the interlayer spacing tend to increase as the deposition rate decreases and the alloy composition moves away from $c_0=0.5$. This phenomenon can be observed in all the simulation temperatures considered in this study.

The above simulation results are used to establish a microstructure map in the space of alloy composition (volume fraction), deposition rate and deposition temperature, as shown in Fig. 4. In order to make the microstructure map applicable to different systems (either model systems considered in a simulation study or real systems investigated in an experiment), it is presented in a normalized parameter space, i.e., the deposition rate $v^N = v/(D_s/\lambda_{max})$ [18] where v is the deposition rate and v is the maximum CM wavelength given by v is the gradient energy coefficients for concentration and v is the second derivative of the local chemical free energy with respect to concentration); the deposition temperature v is the volume fraction v is the second derivative of the local chemical free energy with respect to concentration); the deposition temperature v is the volume fraction v is the volume fraction v is the deposition temperature v is the volume fraction v is the volume v in v is the volume v in v

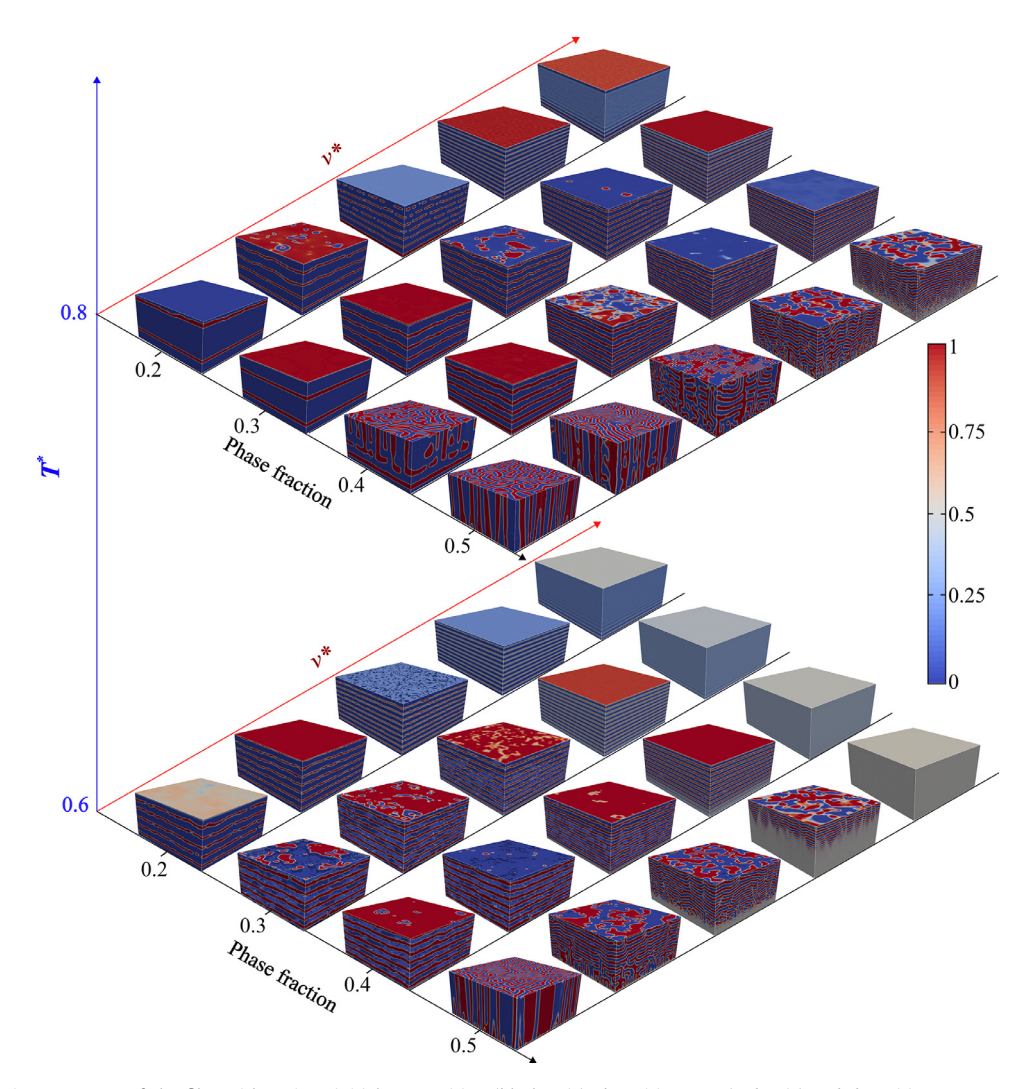


Fig. 3. As-deposited microstructures of the film with various initial composition (black axis), deposition rate (red axis) and deposition temperature (blue axis). At lower temperature and equivalent volume fraction (c0 = 0.5), the film morphology transforms from VCM to LCM, and a non-modulated "frozen" state that gradually develops from the film bottom. When the volume fraction of the A-rich phase increases, VCMs are well developed and perfect multi-layer structure arise. (For interpretation of the references to colour in this figure legend, the reader is referred to the web version of this article.)

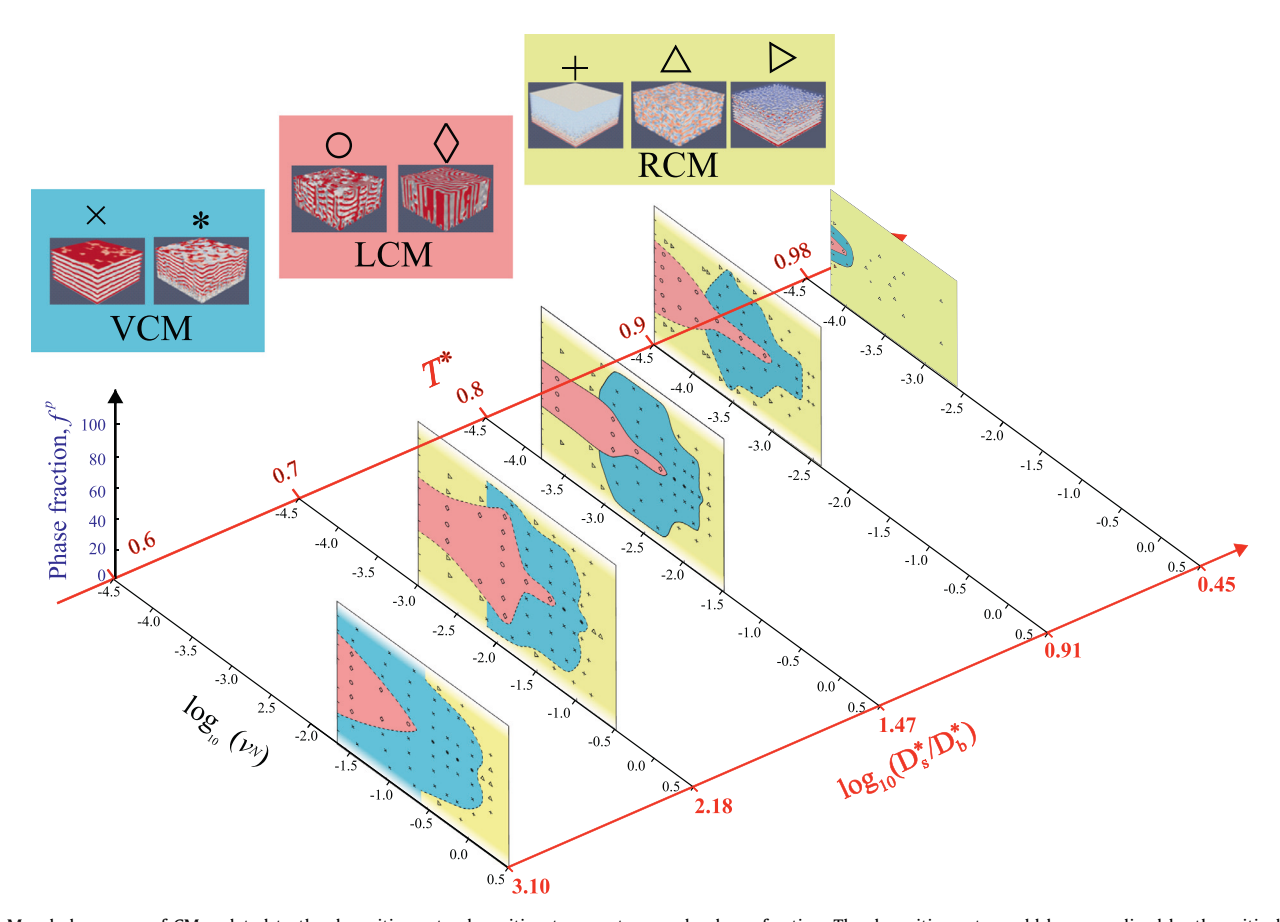


Fig. 4. Morphology map of CMs related to the deposition rate, deposition temperature, and volume fraction. The deposition rate could be normalized by the critical wavelength and surface diffusivity[18], i.e., where v is the real deposition rate. λ max is the maximum wavelength can be written as . Subscribing the parameters used in the simulation, the relationship of normalized deposition rate, volume fraction and the ratio of surface and bulk diffusivity, related to deposition temperature. The symbol x and * denote the multilayer film and multilayer film with "frozen layer" at the bottom, respectively, both of which were treated as VCM. The symbol \diamond and \diamond denote columnar structure and columnar structural film with random interconnected structure at bottom, respectively, both of which were treated as LCM. The symbol +, \diamond and \diamond \diamond 0 denote the homogenous film with bottom layered structure, interconnected structure and discrete particles with bottom layered structure, respectively, all of which were treated as RCM.

two equilibrium compositions of spinodal decomposition). The actual deposition rate of the present simulation was calculated by $v=v^*(l_0/\Delta t)$. By normalizing the parameters $(v,\ T\ \text{and}\ c_0)$ of each simulation, the corresponding CM type can be plotted in the normalized parameter space as shown in Fig. 4. In the microstructure map, the temperature range considered is $0.6 \le T^* \le 0.98$, at which the ratio of surface diffusivity to bulk diffusivity, $D_s^*(T)/D_b^*(T)$, varies from 2500 to 1. The corresponding volume fraction and log (v^N) vary from $0.1{\sim}0.9$ and $-3.5 \sim 1.5$, respectively. The film morphologies (*i.e.*, CM patterns) are categorized into three types: VCM, LCM and RCM, as can be seen in the insets of Fig. 4.

The microstructure map is symmetrical with respect to the volume fraction, with a mirror at volume fraction 50% (note that this is only true for systems with symmetrical miscibility gaps, as the one considered in the current study). Overall, all the microstructural fields, VCM, LCM and RCM, shift towards low deposition rate side as temperature increases. The VCM field shrinks as temperature increases, especially at low and high volume fraction sides. At low temperatures, the VCM field expands towards the direction of low or high deposition rate. When the deposition rate decreases, the LCM field tends to expand to the large or small volume fraction end. These features imply that increasing deposition temperature restrains the VCM structures in cases of large differences in the two volume fractions. When the deposition temperature is close to the critical temperature of spinodal decomposition, the LCM and

VCM fields shrink drastically and appear only at low deposition rates.

Table 2 serves to summarize the characteristic morphologies found in the co-deposited Cu-Mo thin film system. These morphologies are a function of deposition temperature and material flux and may be juxtaposed into homogeneous and heterogeneous. Homogeneous morphologies are defined as exhibiting bicontinuous phases that can be described by one length [16] (e.g. concentration modulation), whereas heterogeneous structures may only be described by many length scales [40] (e.g. grain size, intergranular precipitate diameter, and concentration modulation). The scanning transmission electron microscopy images presented in Table 2 allows for the clear observation of the various phases in the sample as it maps out contrast according to the atomic weight of the species present in the sample. For example, the sample contains only Cu and Mo atoms. Mo is atomically heavier than Cu and regions rich in Mo will appear brighter in a S/TEM images. Table 2 shows that at low deposition rate (0.14 nm/s), the morphology only exhibited a heterogeneous, bimodal structure: bicontinuous LCMs of Cu and Mo surrounding large Cu phases (large dark regions) containing nanoscale precipitates of Mo [40]. For the heterogeneous structures, higher temperature led to coarsening of all length scales. At higher material fluxes (i.e. 0.7 nm/s and 1.4 nm/s), the structure was found to be homogeneous and Cuand Mo-rich phases formed into VCMs. The structural phases are

Table 2Deposition parameters and microstructures of the Cu-Mo thin films. Each image is a high angle annular dark field image, which means that the dark regions represent the element of higher atomic weight. In each image the growth direction is up and the substrate is below the image even though not necessarily imaged.

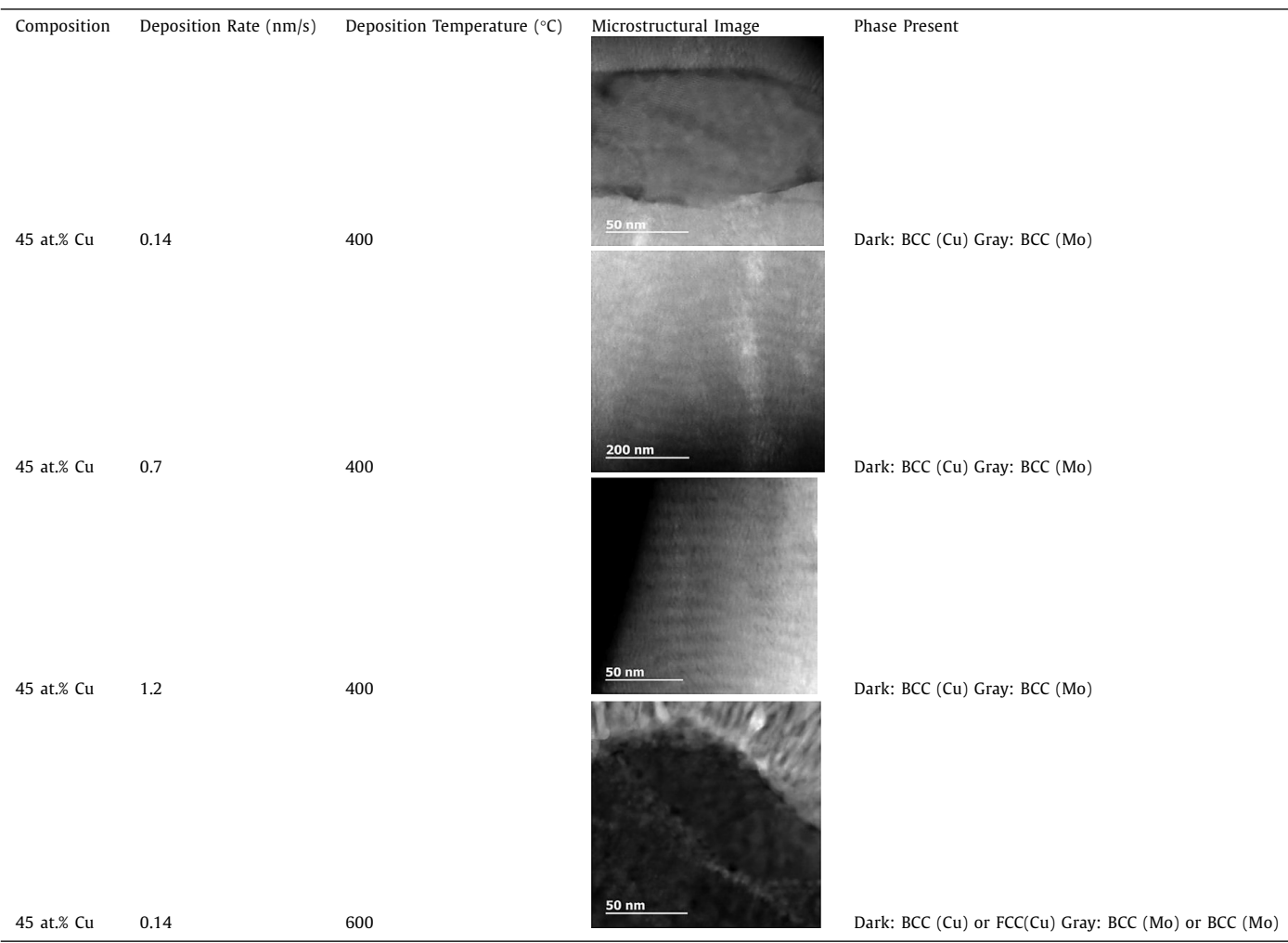


Table 3The parameters used for the normalization of experimental data.

additionally listed in Table 2 and were measured using indexed selected area diffraction patterns, which are not presented here.

The detailed alloy composition, diffusivities, CM wavelengths, deposition rates used for the normalization of the experimental data are listed in Table 3. Based on the experimental results, as well as experimental data available in the literature [16,24], discrete symbols of different colors are placed on the predicted microstructure map (Fig. 5). In order to compare the experimental data with the simulation results, the boundaries between different types of CMs shown in Fig. 4 are projected onto the same figure and represented by different colors, e.g., $T^*=0.6$ (black), 0.7 (orange), 0.8(blue), 0.9(green), 0.98(red), as shown in Fig. 5. The dash and solid lines are respectively for the LCM and VCM fields shown in Fig. 4. It is readily seen that the experimental data are located within each of the CM fields at different temperatures, which coincide well with the microstructure map. This indicates that by accounting for the temperature dependence of the surface and bulk diffusivities and driving force for phase separation, the

simulations predict well the formation of self-organized CM structures fabricated at low temperatures. As the deposition temperature increases, the VCM region at higher deposition rate shrinks, which indicates that the increase in bulk diffusion interrupts the surface layer formation. In addition, the LCM region also shrinks when the deposition rate decreases.

4. Discussion

The formation of different types of CM patterns and transitions between them in the space of alloy composition, deposition rate and deposition temperature are revealed clearly in the computed microstructure map. According to the map, VCM, LCM and RCM structures can be obtained in a broad range of deposition temperatures. Previous studies [18,25,27] have focused on relatively high deposition temperature where bulk diffusion dominates the phase separation process. Without considering the temperature dependence of the thermodynamic parameters in the free energy, both

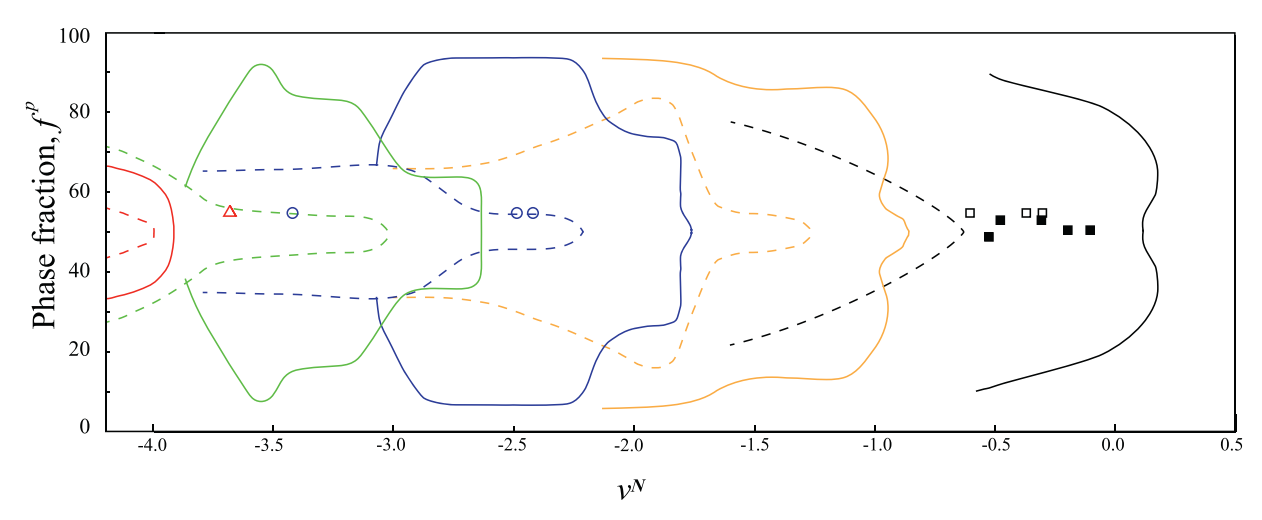


Fig. 5. The projection of microstructure map at different temperatures: $T^* = 0.6$ (black), 0.7 (orange), 0.8(blue), 0.9(green), 0.98(red). The dash and solid lines are the LCM and VCM boundaries shown in Fig. 4, respectively. The normalized experimental data of RCM, LCM and VCM are shown by colored markers, *e.g.*, red triangle is the experimental data of RCM structure at $T^* = 0.98$, which is in the RCM region of $T^* = 0.98$ (red lines); the blue circles are experimental data of LCM structures at $T^* = 0.8$, which are in the LCM region of $T^* = 0.8$ (blue lines); the black squares are experimental data of VCM structures at $T^* = 0.6$, which are in the VCM region of $T^* = 0.6$ (black lines). The empty markers are measured by the present work, while the solid markers are calculated by the literature [16,24]. (For interpretation of the references to colour in this figure legend, the reader is referred to the web version of this article.)

bulk and surface diffusion and the surface energy difference, the VCM structure fabricated at lower temperature in the experiment cannot be predicted. Below we discuss the effects of surface/bulk diffusion and temperature-dependent surface energy, which have not been studied in the literature, as well as the characteristics of the present CM microstructural map in some details.

4.1. Subsurface layer effect under surface diffusion-controlled phase separation

At low temperatures, slow bulk diffusion has insignificant contribution to phase separation, while surface diffusion becomes the only kinetic pathway to yield solute-rich and solute-lean regions. However, there is limited amount of time for surface diffusion to take place during deposition before the surface layer is buried underneath a new surface layer and become the subsurface layer (i.e., bulk). The time interval for surface diffusion to occur could be estimated by the time needed for laying down the entire surface layer, e.g. $\Delta t^s = l_0/v^*$. During this period, the degree of decomposition in the surface layer will depend on the degree of CM developed previously in the subsurface layer. By monitoring the simulated concentration evolution of the surface layers deposited on substrate with various degree CMs, we have obtained the dependence of the required diffusion time to reach certain degrees of phase separation on the degree of CM in the subsurface layer. As shown in Fig. 6, the vertical axis is the maximum subsurface-layer CM, i.e., $\Delta c_{sub}^{max} =$ $c^{max} - c^{min}$, where c^{max} and c^{min} are the maximum and minimum solute concentration of the subsurface layer, and the horizontal axis, t^* , is the diffusion time. $\Delta c_{sub}^{max}=0$ denotes spinodal decomposition in the surface layer without the subsurface-layer effect, i.e., the subsurface layer has identical uniform composition as that of the surface layer. The solid lines with different symbols indicate different degrees of decomposition (i.e., the decomposition rates) in the surface layer, characterized by $\Delta c_{surf}^{max}/\Delta c_{eq}^{max}$, where Δc_{surf}^{max} is the maximum CM of the surface layer and Δc_{eq}^{max} is the maximum CM at equilibrium (i.e., the difference between the equilibrium compositions of the solute-rich and solute-lean phases). It can be readily seen that, for a given degree of decomposition in the surface layer, the diffusion time required decreases with increasing sub-layer concentration modulation.

It is noted that, at low temperatures, the subsurface layer effect can only play a role under the surface-diffusion-controlled case. At the beginning of the deposition process, Δc_{sub}^{max} is close to zero, from Fig. 6(a) we can see that the surface layer needs longer time to reach a given degree of phase separation, then it could already be covered by the newly deposited layer. However, when the subsurface layer has even a small degree of decomposition, the time required for the surface layer to start decomposition is reduced dramatically. This cumulative effect brings larger and larger CMs for the surface layer, which continuously accelerate the decomposition process in the surface layer. In order to show this effect, snapshots of the microstructure at a 2D cross-section right after its transition from the surface layer into the sub-surface layer at different times are presented in Fig. 6(b) and (c). Fig. 6(b) shows the final VCM microstructure obtained in an alloy with a symmetrical composition (i.e., 50%) at a deposition rate of $v^*=2 \times 10^{-3}$ at $T^* = 0.6$. The snapshots of the 2D cross-section microstructures in Fig. 6(b) marked A, B, C, and D are shown in Fig. 6(c). In this case, Δt^s can be calculated based on the deposition rate, e.g. $\Delta t^s = 0.671$. From Fig. 6(a), if we assume that the Δc_{sub}^{max} of the sub-layer for cross-section A is close to zero, then the transformation rate between 10% (line with symbol Δ) and 25% (line with symbol +) could be reached during this time period. Thus, the maximum concentration modulation of cross-section A should be within $10\%\Delta c_{eq}^{max} \sim 25\%\Delta c_{eq}^{max}$, that is $0.1 \sim 0.25$. For cross-section A, $\Delta c_{surf}^{max} = 0.225$, which is within the predicted range of transformation rate, indicating that the sub-surface effect shown Fig. 6(a) coincide with our simulation results. After deposition of 5 layers (h= 10 l_0), Δc_{surf}^{max} of Section B has remarkably reached 0.95.The decomposition of layers beneath section B is rather slow because of the slow bulk diffusion and can be regarded as "frozen" layers that have been observed in different kinds of as-deposited films [41-43]. The solute-rich and solute-lean concentrations in Section C and D are closer to the equilibrium ones, and the CM wavelengths are also much larger. With the help of fast surface diffusion in the new deposited layer, those A-rich and B-rich domains on the surface layer can grow horizontally and lead to the formation

From the simulation results, it can be readily seen that the VCM structure tends to appear at lower deposition temperature in alloys with large differences between the equilibrium volume fractions of

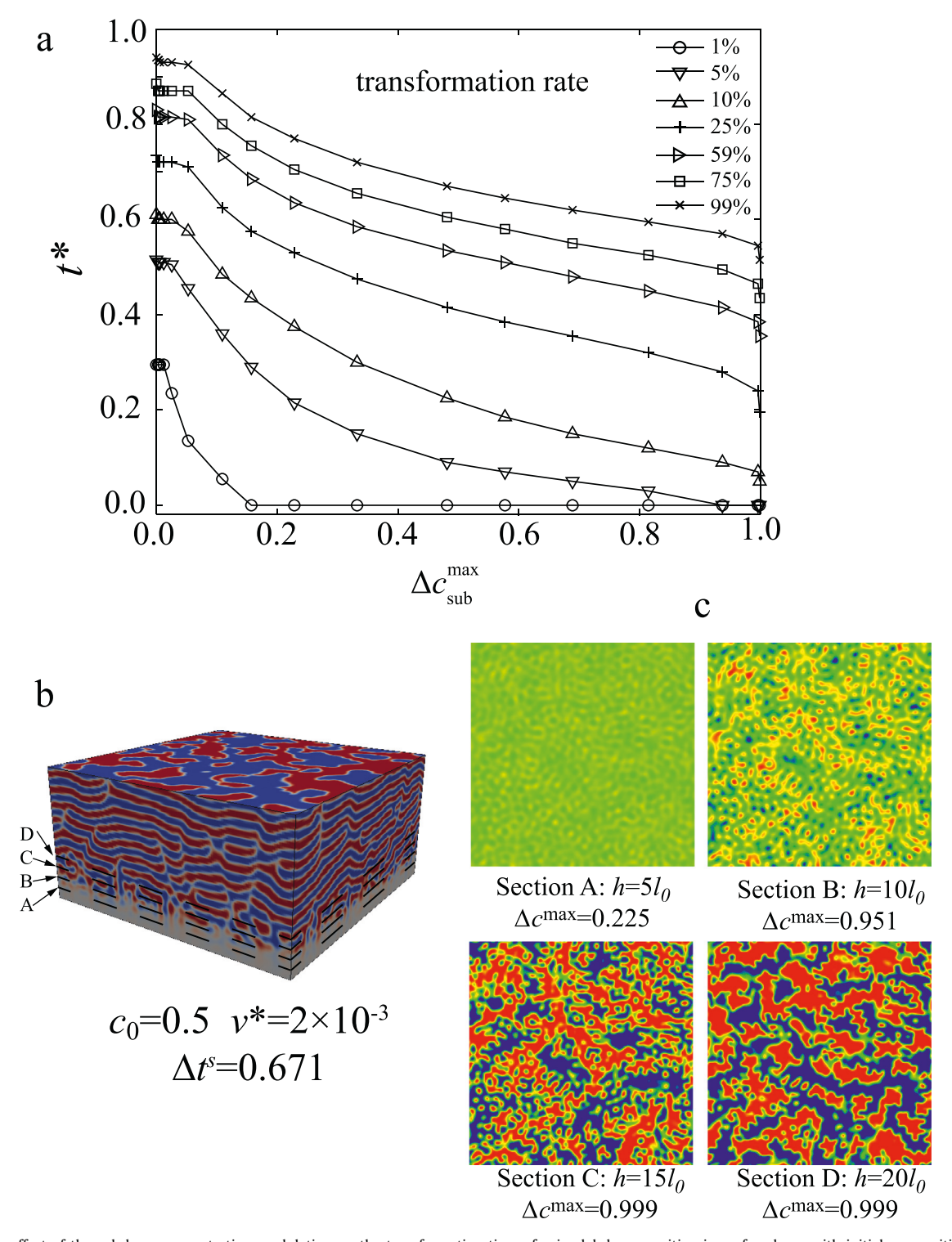


Fig. 6. (a) The effect of the sub-layer concentration modulation on the transformation time of spinodal decomposition in surface layer with initial composition of 0.5. The maximum sub-layer concentration modulation, =cmax - cmin, where cmax and cmin are the maximum and minimum concentration of the sub-surface layer. (b) and (c) show the 3D simulated final microstructure and the instantaneous microstructures of cross-section right after transition into sub-surface layer.

the two phases (*i.e.*, away from 50%). Previous studies have suggested that the formation of the VCM structure during film deposition is through either coarsening of an intermediate "chessboard" structure [18] or continuous domain formation at fast deposition rates [23]. Therefore, the VCM formation in alloys with volume fractions far away from 50% (*e.g.*, < 40% in Ref. [16]) cannot be predicted without considering the effects of surface diffusion and surface energy of the film.

4.2. Effect of surface energy

When the initial composition of the film deviates from the symmetrical one (*i.e.*, 0.5), in the surface layer, any small concentration fluctuation will not only induce spontaneous spinodal decomposition, but also result in surface energy differences between the solute-lean and solute-rich areas. According to the energy profile shown in Fig. 1, the surface energies for the two equilibrium

phases are the same and the lowest, while the surface energies of any surface areas that have compositions in between the two equilibrium compositions are larger than that of the ones with equilibrium compositions and are different from each other if their compositions are not symmetrical to 0.5. Thus, for an initial composition of 0.5, the surface energy has no remarkable effect on the microstructure evolution in the surface layer because the soluterich and solute-lean concentrations are symmetrical with respect to 0.5. However, when the initial alloy composition is off symmetrical (i.e., either lower or higher than 0.5), the equilibrium phase having a composition close to the initial alloy composition always tends to wet the surface [25] because in the initial CM the one that is farther away from the symmetrical composition has lower surface energy. In addition, due to the temperature-dependent energy hump of the spinodal decomposition, the surface energy decreases with increasing temperature. This surface-directed spinodal decomposition effect [29] enhances the development of the VCM structure during film deposition.

Figs. 7 (a-g) show the schematic evolution of the layer structure during deposition with the effect of composition-dependent surface energy. The deposition process could be treated as two steps: deposition and diffusion in a small time interval (Δt^s). In our simulations, we assume surface diffusion occurs only within a small thickness (h_s) at the top of the film. At the beginning of deposition, due to the surface energy effect, the phase with lower surface energy (e.g., the A-rich phase) tend to wet the film surface. During the following step of deposition, within the subsurface layer, the Arich layer continues to grow by rejecting B atoms, result in the formation of a B-rich layer at the surface. When the B-rich layer occupies the whole surface area and grows by absorbing B atoms near the surface, the A-rich layer underneath stops growth because A atoms are difficult to diffuse through the B-rich layer. Then, within the surface layer, A atoms begin to accumulate to the film surface again. For faster deposition rate, the growth of the A-rich layer at the film surface will be terminated sooner, leading to a decreasing CM wavelength with increasing deposition rate. It should be noted that, at higher temperature, even the A-rich phase has lower surface energy and prefer to form at the surface layer, the later coarsening effect via faster bulk diffusion can interrupt the layered growth process. At lower temperature, the slow bulk diffusion is unable to alter these layered structures formed at the surface area. Therefore, the VCM regions shown in Fig. 4 shrink with the increasing of deposition temperature.

4.3. Deviation from the equilibrium volume fractions in VCM structures

As can be seen from Fig. 3, both the compositions and volume fractions of the two phases in the VCMs produced under fast deposition rates and with film compositions far away from 0.5 are far from their equilibrium values. When the film composition is far away from 0.5, the two phases have large difference in their volume fractions and the average film composition is always far away from the equilibrium composition of one of the two phases. At lower deposition temperature and in the case of fast deposition rate, the spinodal decomposition only occurs in the surface layer that is quickly covered by the freshly deposited layer. Thus, the phase that has its equilibrium composition far away from the film composition (i.e., the average composition of the film) has no time to reach its equilibrium composition and thus its equilibrium volume fraction. The composition of the other phase may not be able to reach its equilibrium value either, but much closer to it. The comparison of different concentration profiles of two time steps (t^* = 30 and 50) with T^* = 0.6 is shown in Fig. 8. It can be obviously seen that, the maximum concentration is far away from the equilibrium composition (\sim 1.0) and the decomposition only occurs

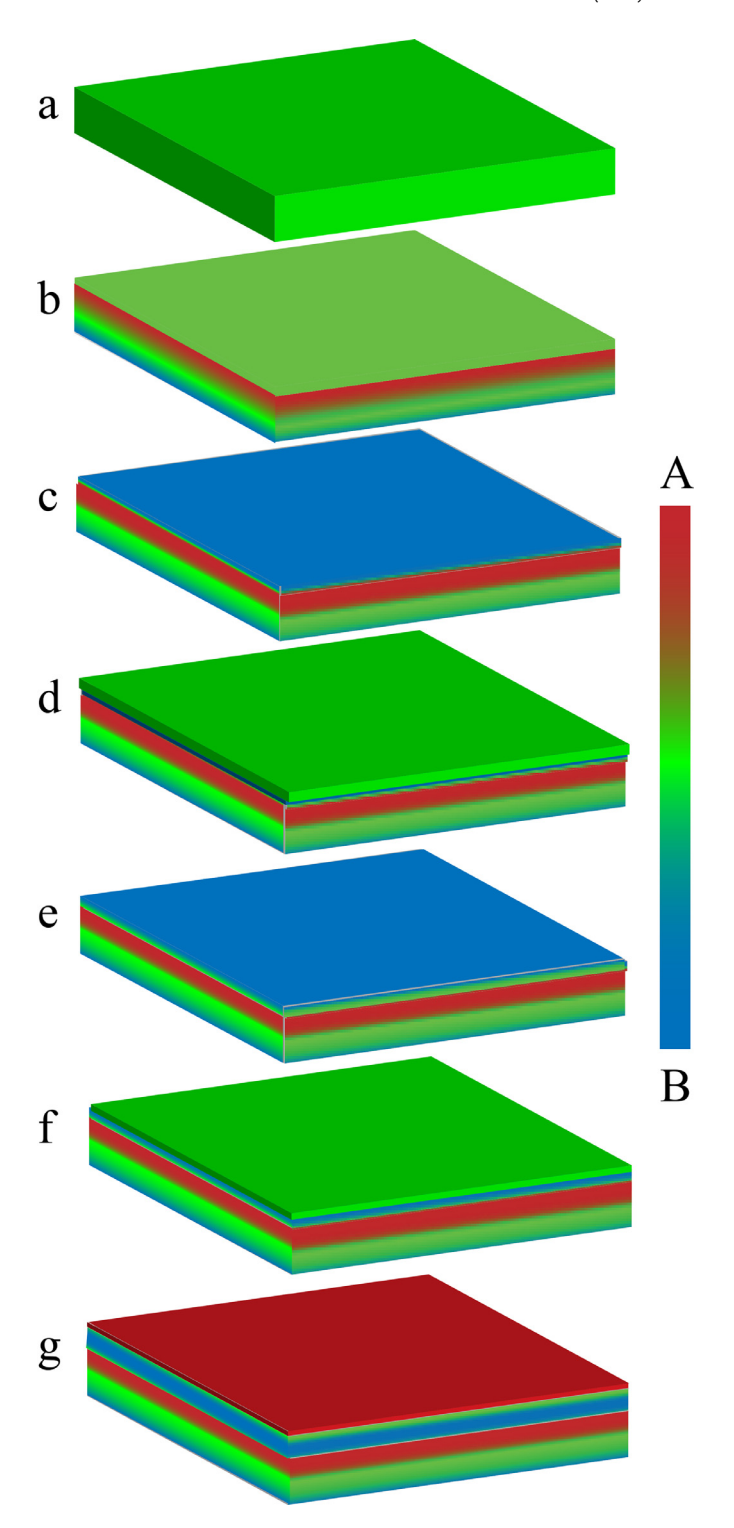


Fig. 7. The schematic evolution of layer structure during the deposition with surface energy effect.

in the surface layer. For slower deposition rates, because of the longer surface diffusion times allowed for each of the freshly deposited layers, both phases may have enough time to reach their equilibrium compositions. Hence, under slow deposition rate, the wavelength of the CM is larger than that under faster deposition rate. This agrees with Daruka and Tersoff's study [25] showing that the wavelength of the self-organized layer structure increases with decreasing deposition rate. For deposition at higher temperatures, with the aid of bulk diffusion, the domains for the phase with

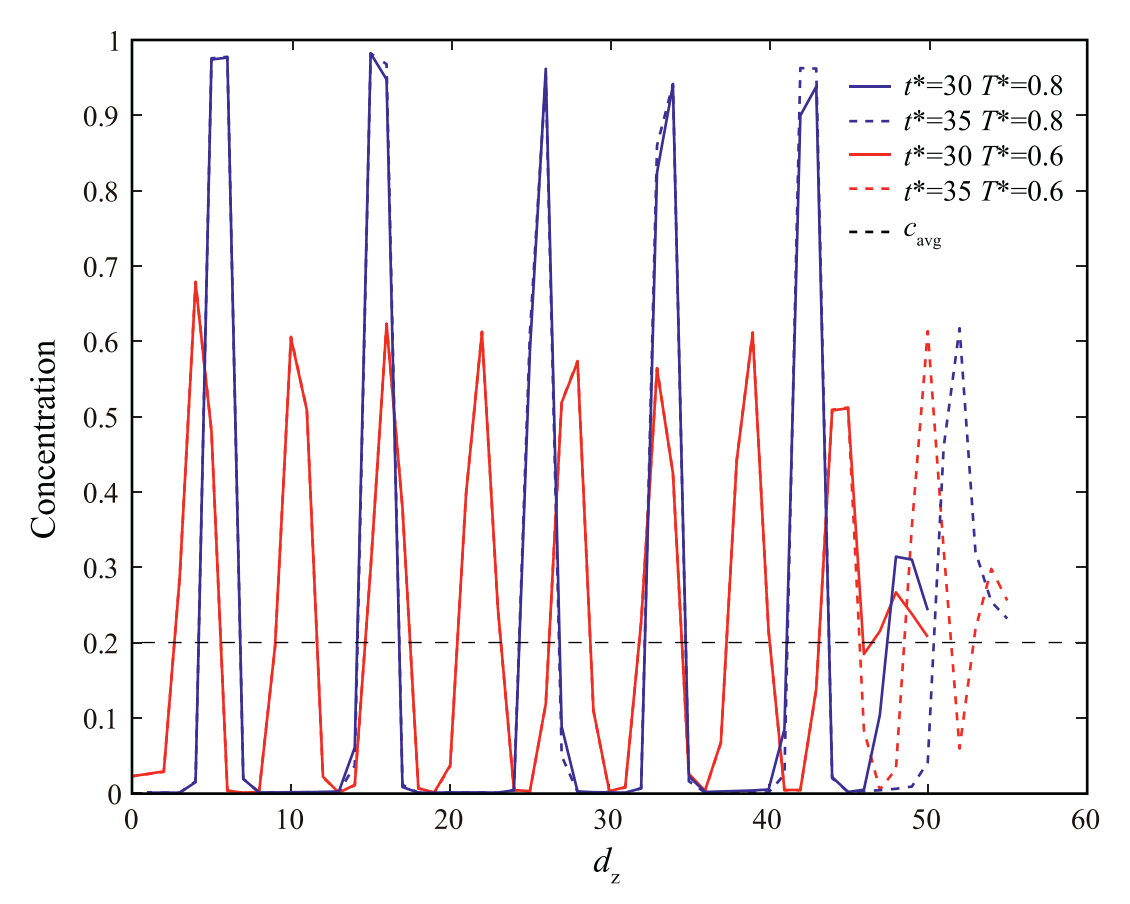


Fig. 8. The concentration profiles along vertical direction for the film with deposition rate $v^* = 0.002$. The black dash line is the average composition of the film. The blue dash and solid lines are the concentration wave of $t^* = 30$ and 50 with deposition temperature $T^* = 0.8$. The red dash and solid lines are the concentration wave of $t^* = 30$ and 50 with deposition temperature $T^* = 0.6$. (For interpretation of the references to colour in this figure legend, the reader is referred to the web version of this article.)

smaller volume fraction in the surface area can connect and evolve to a horizontal layer.

In addition, for the film with average composition close to 0.5, the volume fraction of the red phase for higher temperature (as shown in Fig. 3) is smaller than that of the low temperature (since the equilibrium compositions are closer to 0.5 at high temperature, as seen in the energy surface in Fig. 1). For small deposition rate and initial composition away from 0.5, the wavelength of CM at higher temperature deposition is different from that at lower temperature deposition, as can be seen from Fig. 8. Because the fastest growth wavelength of spinodal decomposition is determined by energy hump (ΔG) and gradient energy coefficient (κ_c), when considering a strong temperature dependent ΔG , the fastest growth wavelength increases with increasing temperature, i.e. the lower the temperature, the smaller of the wavelength. Thus, when considering the temperature dependent chemical free energy, surface diffusion and surface energy effect, the wavelength of VCM increases with increasing of both temperature and deviation of volume fractions.

4.4. Effect of deposition temperature on the microstructural map

By considering the temperature dependence of the local chemical free energy, surface diffusion and bulk diffusion, we have found the LCM and VCM fields in the microstructure map could shift and expand significantly. At lower temperatures, the coupling of the surface diffusion and surface energy effect expands the VCM region towards the two sides of the equilibrium volume fraction, while the LCM region shrinks to an area of slower deposition rate and smaller deviation of the volume fraction from the symmetri-

cal 50/50. As temperature increases, the bulk diffusion increases. The sub-surface layer can participate in the decomposition process near the film surface, which gives rise to a continuous growth of the A-rich or B-rich domains along the vertical direction with the aid of surface diffusion. This effect shifts the LCM region towards faster deposition rate and reduces the VCM region. The growth of the columnar structure (LCM) needs a continuous growth of both phases at the film surface. However, a smaller volume fraction (\sim 35%) is not likely to maintain the uninterrupted growth of the phase with smaller volume fraction. At lower temperature, the short time interval for surface diffusion cannot maintain the continuous growth of the columnar structure, leading to layers with incomplete coverage of B-rich layer (with A-rich domains inside the layer, we call them as LCM). Thus, when the deposition rate decreases, the LCM region enlarges near the symmetrical composition of 0.5. As temperature increases, the coarsening effect destroys the columnar structure at slow deposition rate. The boundary of LCM area moves to the equilibrium volume fraction direction.

5. Summary

In summary, by considering the temperature-dependent driving force and surface and bulk diffusivities, and composition-dependent surface energy, we have constructed a CM microstructure map for thin film deposition in a multi-dimensional space of material properties and processing parameters using computer simulations based on the phase field method. The CM microstructure patterns and morphological transition sequences in as-deposited films predicted by the microstructure map agree well

with experimental data from sputtered alloy films. The major findings are summarized below.

- (1) The VCM, LCM and RCM structures can be obtained in a broad range of deposition temperatures. The VCM and LCM regions shift towards low deposition rate side as temperature increases. At low temperatures, the VCM field expands in the direction of high deposition rate. The VCM field shrinks as temperature increases, especially on the low and high volume fraction sides.
- (2) At lower temperatures, when the bulk diffusion is negligible relative to the deposition rate, surface diffusion is the only kinetic pathway for phase separation. Small degree of decomposition in the subsurface layer could dramatically reduce the time required for the surface layer to start decomposition. The cumulative effect of concentration modulation developed in the subsurface layer expedites the subsequent phase separation process at the surface, leading to VCM structures.
- (3) When the initial alloy composition is off the center of the miscibility gap (i.e., smaller or larger than 0.5), the equilibrium phase close to the initial alloy composition always tend to wet the surface and, thus, help the development of CMs along the vertical direction. This effect could be enhanced via surface diffusion at lower temperature and facilitate the formation of VCM at lower temperatures.
- (4) Due to incomplete decomposition in VCM structure at lower temperature, films with compositions off the center of the miscibility gap could have different wavelength (period of the VCM structure) from that seen in spinodal decomposition in the bulk. When considering the temperature-dependent surface diffusion and surface energy effect, the wavelength of VCM increases with increasing temperature and deviation of film composition from the center of the miscibility gap.
- (5) As temperature increases, the contribution of bulk diffusion and decrease in driving force for spinodal decomposition gradually diminish the contribution from surface diffusion. The formations of VCM and LCM are interrupted, resulting in the shrinkage of their corresponding fields in the microstructure map.

Since the CM microstructure map is constructed using normalized deposition rate and temperature, it is general and can be used to guide the synthesis of both semiconductor and metal films for desired CM patters.

Declaration of Competing Interest

None.

Acknowledgements

YL would like to thank the financial support by National Key R&D Program of China (2017YFB0702401), Natural Science Foundation of Fujian Province of China (2019J01033) and the China Scholarship Council (Grant No.201806315068). AM and BD acknowledge support from the Center for Research Excellence on Dynamically Deformed Solids (CREDDS) sponsored by the Department of Energy—National Nuclear Security Administration (DOENNSA), Stewardship Science Academic Program under Award No. DE-NA0003857. YW acknowledge support from the Natural Science Foundation under Grant No. DMR-1923929.

References

- [1] L. Li, Y. Yu, G.J. Ye, Q. Ge, X. Ou, H. Wu, D. Feng, X.H. Chen, Y. Zhang, Black phosphorus field-effect transistors, Nat. Nanotechnol. 9 (2014) 372.
- [2] J.G. Song, G.H. Ryu, S.J. Lee, S. Sim, C.W. Lee, T. Choi, H. Jung, Y. Kim, Z. Lee, J.M. Myoung, C. Dussarrat, C. Lansalot-Matras, J. Park, H. Choi, H. Kim, Controllable synthesis of molybdenum tungsten disulfide alloy for vertically composition-controlled multilayer, Nat. Commun. 6 (1) (2015) 7817.

[3] S. Kim, S. Zhou, Y. Hu, M. Acik, Y.J. Chabal, C. Berger, W. de Heer, A. Bongiorno, E. Riedo, Room-temperature metastability of multilayer graphene oxide films, Nat. Mater. 11 (6) (2012) 544–549.

- [4] R.E. Simpson, P. Fons, A.V. Kolobov, T. Fukaya, M. Krbal, T. Yagi, J. Tominaga, Interfacial phase-change memory, Nat. Nanotechnol. 6 (8) (2011) 501–505.
- [5] J.A. Rogers, T. Someya, Y. Huang, Materials and mechanics for stretchable electronics, Science 327 (5973) (2010) 1603.
- [6] H. Ko, K. Takei, R. Kapadia, S. Chuang, H. Fang, P.W. Leu, K. Ganapathi, E. Plis, H.S. Kim, S.Y. Chen, M. Madsen, A.C. Ford, Y.L. Chueh, S. Krishna, S. Salahuddin, A. Javey, Ultrathin compound semiconductor on insulator layers for high-performance nanoscale transistors, Nature 468 (7321) (2010) 286–289.
- [7] D.B. Mitzi, L.L. Kosbar, C.E. Murray, M. Copel, A. Afzali, High-mobility ultrathin semiconducting films prepared by spin coating, Nature 428 (6980) (2004) 299–303.
- [8] M.J. Demkowicz, Does shape affect shape change at the nanoscale? Mrs Bull. 44 (1) (2019) 25–30.
- [9] D. Chen, N. Li, D. Yuryev, J.K. Baldwin, Y. Wang, M.J. Demkowicz, Self-organization of helium precipitates into elongated channels within metal nanolayers, Sci. Adv. 3 (11) (2017) eaao2710.
- [10] J.S. Bangsund, T.R. Fielitz, T.J. Steiner, K. Shi, J.R. Van Sambeek, C.P. Clark, R.J. Holmes, Formation of aligned periodic patterns during the crystallization of organic semiconductor thin films. Nat. Mater. 18 (7) (2019) 725–731.
- of organic semiconductor thin films, Nat. Mater. 18 (7) (2019) 725–731.
 [11] J. Peet, A.J. Heeger, G.C. Bazan, Plastic" solar cells: self-assembly of bulk heterojunction nanomaterials by spontaneous phase separation, Acc. Chem. Res. 42 (11) (2009) 1700–1708.
- [12] J.R. Simon, N.J. Carroll, M. Rubinstein, A. Chilkoti, G.P. López, Programming molecular self-assembly of intrinsically disordered proteins containing sequences of low complexity, Nat. Chem. 9 (6) (2017) 509–515.
- [13] J.L. MacManus-Driscoll, Self-assembled heteroepitaxial oxide nanocomposite thin film structures: designing interface-induced functionality in electronic materials, Adv. Funct. Mater. 20 (13) (2010) 2035–2045.
- [14] S. Gallardo-Hernández, I. Martinez-Velis, M. Ramirez-Lopez, Y. Kudriatsev, A. Escobosa-Echavarria, S.L. Morelhao, M. Lopez-Lopez, Self-assembly of compositionally modulated Ga_{1-x}Mn_xAs multilayers during molecular beam epitaxy, Appl. Phys. Lett. 103 (19) (2013) 192113.
- [15] J. Zalesak, D. Holec, I. Matko, M. Petrenec, B. Sartory, N. Koutná, R. Daniel, R. Pitonak, J. Keckes, Peculiarity of self-assembled cubic nanolamellae in the TiN/AlN system: Epitaxial self-stabilization by element deficiency/excess, Acta Mater. 131 (131) (2017) 391-399.
- [16] B. Derby, Y. Cui, J.K Baldwin, A. Misra, Effects of substrate temperature and deposition rate on the phase separated morphology of co-sputtered, Cu-Mo thin films, Thin Solid Films 647 (2018) 50–56.
- [17] K. Fukutani, K. Tanji, T. Saito, T. Den, Phase-separated Al-Si thin films, J. Appl. Phys. 98 (3) (2005) 033507.
- [18] Y. Lu, C.P. Wang, Y.P. Gao, R.P. Shi, X.J. Liu, Y.Z. Wang, Microstructure map for self-organized phase separation during film deposition, Phys. Rev. Lett. 109 (8)
- [19] B.G. Chirranjeevi, T.A. Abinandanan, M.P. Gururajan, A phase field study of morphological instabilities in multilayer thin films, Acta Mater. 57 (4) (2009) 1060–1067.
- [20] R. Raghavan, A. Mukherjee, K. Ankit, Nanostructural evolution in vapor deposited phase-separating binary alloy films of non-equimolar compositions: Insights from a 3D phase-field approach, J. Appl. Phys. 128 (17) (2020) 175303.
- [21] E. Luna, M. Wu, M. Hanke, J. Puustinen, M. Guina, A. Trampert, Spontaneous formation of three-dimensionally ordered Bi-rich nanostructures within GaAs_{1-x}Bi_x/GaAs quantum wells, Nanotechnology 27 (32) (2016) 325603.
- [22] J.L. MacManus-Driscoll, A. Suwardi, H. Wang, Composite epitaxial thin films: a new platform for tuning, probing, and exploiting mesoscale oxides, Mrs Bull. 40 (11) (2015) 933–942.
- [23] K. Ankit, B. Derby, R. Raghavan, A. Misra, M.J. Demkowicz, 3-D phase-field simulations of self-organized composite morphologies in physical vapor deposited phase-separating binary alloys, J. Appl. Phys. 126 (7) (2019) 075306.
- [24] T. Xie, L. Fu, X. Cao, J. Zhu, W. Yang, D. Li, L. Zhou, Self-assembled binary immiscible Cu-transition metal multilayers prepared by co-sputtering deposition, Thin Solid Films 705 (2020) 138037.
- [25] I. Daruka, J. Tersoff, Self-Assembled Superlattice by Spinodal decomposition during growth, Phys. Rev. Lett. 95 (7) (2005) 076102.
- [26] Y.W. Yen, Y.L. Kuo, J.Y. Chen, C. Lee, C.Y. Lee, Investigation of thermal stability of Mo thin-films as the buffer layer and various Cu metallization as interconnection materials for thin film transistor-liquid crystal display applications, Thin Solid Films 515 (18) (2007) 7209–7216.
- [27] J.A. Stewart, R. Dingreville, Microstructure morphology and concentration modulation of nanocomposite thin-films during simulated physical vapor deposition, Acta Mater. 188 (2020) 181–191.
- [28] R.P. Shi, C.P. Wang, D. Wheeler, X.J. Liu, Y. Wang, Formation mechanisms of self-organized core/shell and core/shell/corona microstructures in liquid droplets of immiscible alloys, Acta Mater. 61 (4) (2013) 1229–1243.
- [29] R.A.L. Jones, L.J. Norton, E.J. Kramer, F.S. Bates, P. Wiltzius, Surface-directed spinodal decomposition, Phys. Rev. Lett. 66 (10) (1991) 1326–1329.
- [30] J.W. Cahn, H.E. Hilliard, Free energy of a nonuniform system. I. interface free energy, J. Chem. Phys. 28 (2) (1958) 258–267.
- [31] J.W. Cahn, On spinodal decomposition, Acta Metall. 9 (1961) 795-801.
- [32] S.M. Allen, J.W. Cahn, Ground state structures in ordered binary alloys with second neighbor interactions, Acta Metall. 20 (3) (1972) 423–433.
- [33] D. Srinivasan, S. Sanyal, R. Corderman, P.R. Subramanian, Thermally stable nanomultilayer films of Cu/Mo, Metall. Mater. Trans. A 37 (3) (2006) 995–1003.

[34] S.M. Wise, J.S. Kim, W.C. Johnson, Surface-directed spinodal decomposition in a stressed, two-dimensional, thin film, Thin Solid Films 473 (1) (2005) 151–163.

- [35] W.L. Chan, E. Chason, Making waves: kinetic processes controlling surface evolution during low energy ion sputtering, J. Appl. Phys. 101 (12) (2007) 121301.
- [36] Z.Q. Liu, Scale space approach to directional analysis of images, Appl. Opt. 30 (11) (1991) 1369–1373.
- [37] C.A. Schneider, W.S. Rasband, K.W. Eliceiri, NIH image to image]: 25 years of image analysis, Nat. Methods 9 (7) (2012) 671–675.
 [38] M.A. Morris, C.J. Barnes, D.A. King, Monolayer and multilayer surface diffusion,
- [38] M.A. Morris, C.J. Barnes, D.A. King, Monolayer and multilayer surface diffusion, growth mode and thermal stability of indium on W {100}, Surf. Sci. 173 (2) (1986) 618–638.
- [39] I. Beszeda, E.G. Gontier-Moya, D.L. Beke, Investigation of mass transfer surface self-diffusion on palladium, Surf. Sci. 547 (1) (2003) 229–238.
- [40] B. Derby, Y. Cui, J. Baldwin, R. Arróyave, M.J. Demkowicz, A. Misra, Processing of novel pseudomorphic Cu–Mo hierarchies in thin films, Mater. Res. Lett. 7 (1) (2019) 1–11.
- [41] F.T.N. Vüllers, R. Spolenak, From solid solutions to fully phase separated interpenetrating networks in sputter deposited "immiscible" W-Cu thin films, Acta Mater. 99 (2015) 213–227.
- [42] A.G. Norman, S.P. Ahrenkiel, H.R. Moutinho, C. Ballif, M.M. Al-Jassim, A. Mascarenhas, D.M. Follstaedt, S.R. Lee, J.L. Reno, E.D. Jones, J. Mirecki-Millunchick, R.D. Twesten, The nature and origin of lateral composition modulations in short-period strained-layer superlattices, MRS Proc. 583 (1) (1999) 297–313.
- [43] G. Abrasonis, G.J. Kovács, M.D. Tucker, R. Heller, M. Krause, M.C. Guenette, F. Munnik, J. Lehmann, A. Tadich, B.C.C. Cowie, L. Thomsen, M.M.M. Bilek, W. Möller, Sculpting nanoscale precipitation patterns in nanocomposite thin films via hyperthermal ion deposition, Appl. Phys. Lett. 97 (16) (2010) 163108.